

Chromium-doped forsterite: dispersion measurement with white-light interferometry

Isabell Thomann, Leo Hollberg, Scott A. Diddams, and Randy Equall

Using a Michelson white-light interferometer, we measure the group-delay dispersion and third-order dispersion coefficients, $d^2\phi/d\omega^2$ and $d^3\phi/d\omega^3$, of chromium-doped forsterite ($\text{Cr:Mg}_2\text{SiO}_4$) over wavelengths of 1050–1600 nm for light polarized along both the c and b crystal axes. In this interval, the second-order dispersion for the c axis ranges from 35 fs^2/mm to $-14 \text{ fs}^2/\text{mm}$, and the third-order dispersion ranges from 36 fs^3/mm to 142 fs^3/mm . For the b axis the second-order dispersion ranges from 35 fs^2/mm to $-15 \text{ fs}^2/\text{mm}$ and the third-order from 73 fs^3/mm to 185 fs^3/mm . Our data are relevant for the development of optimized dispersion compensation tools for $\text{Cr:Mg}_2\text{SiO}_4$ femtosecond lasers. These measurements help to clarify previously published results and show some significant discrepancies that existed, especially in the third-order dispersion. Our results should furthermore be useful to build up an analytic expression for the index of refraction of chromium forsterite.

OCIS codes: 120.3180, 160.4760, 160.3380, 320.7160, 320.0320, 140.4050.

1. Introduction

Chromium-doped forsterite ($\text{Cr:Mg}_2\text{SiO}_4$, or simply Cr:forsterite) is a tunable laser material that covers the spectral range from approximately 1170 to 1350 nm. Laser action in Cr:forsterite was first observed in 1988.¹ Soon thereafter, subpicosecond pulses were generated from Cr:forsterite by active mode locking² and additive-pulse mode locking.³ This initiated a wealth of experimental research, including regenerative mode locking,⁴ self-mode locking,^{5,6} an all-solid-state Cr:forsterite femtosecond laser,⁷ and a double-clad fiber-pumped Cr:forsterite femtosecond laser.⁸ Self-starting femtosecond mode locking has been obtained through use of semiconductor saturable absorbers.⁹

Cr:forsterite has been recognized as having potential value in biological imaging because of the reduced scattering length of biological samples in its wavelength region.^{10,11} Other emerging applications of

mode-locked Cr:forsterite lasers include optical frequency metrology¹² and the phase locking of separate mode-locked lasers based in different spectral regions. The principle of this last technique has recently been demonstrated by Shelton *et al.*¹³ and could lead to the development of ultrabroadband coherent sources for applications in optical frequency metrology and ultrafast spectroscopy. Progress in this new direction was made by the recent demonstration of two-color self-synchronized femtosecond Ti:sapphire and Cr:forsterite lasers.¹⁴ For all these applications, ultrashort pulses are desirable, with 14 fs being the shortest pulses reported to date.¹⁵

Generation of the shortest femtosecond pulses requires accurate dispersion data for Cr:forsterite. To our knowledge, there is only one recent measurement of the index of refraction of Cr:forsterite at different wavelengths from which the required dispersion could be computed.¹⁶ All other dispersion data for Cr:forsterite have previously been presented in the context of femtosecond pulse generation.^{4,6,9,17–19} Among many of these, we found significant discrepancies. Furthermore, the information about the specific crystal axis along which measurements have been performed is not easily interpreted in all cases, and unconventional notation has been used in others. Although careful dispersion compensation was used in the recent generation of 14-fs pulses,¹⁵ the authors of that paper did not provide quantitative dispersion data for Cr:forsterite that would be useful to others.

To make accurate dispersion data available that

At the time of this research, I. Thomann (isabell.thomann@colorado.edu), L. Hollberg, and S. A. Diddams (sdiddams@boulder.nist.gov) were with the National Institute of Standards and Technology, 325 Broadway, Boulder, Colorado 80305. R. Equall is with Scientific Materials, 310 Icepond Road, P.O. Box 786, Bozeman, Montana 59715. I. Thomann is now with JILA, University of Colorado, Campus Box 440, Boulder, Colorado 80309-0440.

Received 22 August 2002; revised manuscript received 16 December 2002.

0003-6935/03/090001-06\$15.00/0

allow for broadband dispersion compensation, we performed an independent determination of the group-delay dispersion (GDD) and third-order dispersion (TOD) of Cr:forsterite with a white-light Michelson interferometer. As we show, our GDD results are found to be in reasonably good agreement with recent measurements at one specific wavelength,^{6,17} as well as the data of Zhang *et al.*^{9,19} that span a range of wavelengths. However, discrepancies at the 50% level persist between our TOD data and the data of Zhang *et al.*^{9,19} Because TOD is presently the limiting dispersion in most Cr:forsterite lasers, it is important to have the most accurate value possible to optimally design such a laser. The data of the recent determination of refractive-index dispersion for Cr:forsterite by use of minimum-deviation measurements¹⁶ show little agreement with any of the other studies, including ours.

2. White-Light Interferometer

Because of the broad spectral distribution available from quartz-halogen lamps, the coherence time of the white light is of the order of 1 fs, and for linear spectroscopy the white light behaves in many respects like broadband femtosecond pulses. The white-light technique for measurement of dispersion was first presented by Naganuma *et al.*,²⁰ and the specific measurement system employed is similar to what we have described in detail previously.^{21,22} The light source is a halogen lamp that emits light from 400 nm to at least the detector limit of 1750 nm. The light is collimated by an achromatic lens of a focal length of 15 cm and is directed into a simple Michelson interferometer, consisting of a beam splitter, two mirrors, and a compensator plate. The beam splitter is a thin metallic coating deposited on a fused-silica substrate. In an attempt to balance the dispersion in the two arms of the interferometer, the compensator plate is also made of fused silica and has the same thickness as the beam-splitter substrate. The two mirrors are identical broadband metal reflectors. One of the mirrors is fixed on a translation stage that can be moved by a voice coil. The Cr:forsterite sample, for which we determine the dispersion, is also placed in one of the arms of the interferometer.

At the output of the interferometer, the white-light interference pattern is visible by eye, and maximizing the width of the spatial interference fringes ensures optimal alignment of the interferometer mirrors. The interferogram that is created when the movable mirror is scanned is detected by an InGaAs p.i.n. photodiode and subsequently digitized with an oscilloscope. The InGaAs photodiode is chosen because of its broad spectral response and high sensitivity around 1300 nm, where information about the dispersion is desired. Interferograms are recorded for a balanced interferometer (without the Cr:forsterite sample) and an unbalanced Michelson interferometer (with the Cr:forsterite sample).²¹ In all cases, a helium-neon (He-Ne) laser beam is also sent through the interferometer, and its fringes serve to

calibrate the relative position of the movable mirror. The 632.8-nm He-Ne fringes are similarly detected with a silicon p.i.n. photodiode and digitized on a second channel of the oscilloscope.

3. Data Analysis

We now briefly summarize how one obtains the desired dispersion information from the measured interferogram. The Fourier transform of the measured balanced interferogram yields

$$\tilde{S}_1(\omega) = |S_1(\omega)|\exp[i\phi_1(\omega)]. \quad (1)$$

Ideally, the argument of the exponent is zero, but in reality small differential phase shifts between the two interferometer arms result in $\phi_1(\omega) \neq 0$. If one then inserts the Cr:forsterite sample in one of the interferometer arms, one obtains a new interferogram, which when Fourier transformed yields

$$\tilde{S}_2(\omega) = |S_2(\omega)|\exp[i\phi_2(\omega)]. \quad (2)$$

Dividing Eq. (2) by Eq. (1) yields the relative transmission spectrum and the phase shift $\phi_{Cr} = 2k(\omega)L$ ($2L$ is twice the crystal thickness) between the interferometer arms because of the dispersive properties of the Cr:forsterite crystal:

$$\phi_{Cr}(\omega) = \phi_2(\omega) - \phi_1(\omega). \quad (3)$$

The spectral phase can then be Taylor expanded around the angular frequency ω_0 corresponding to $\lambda = 1.3 \mu\text{m}$:

$$\begin{aligned} \phi_{Cr}(\omega) = & \phi_0 + \phi'|_{\omega_0}(\omega - \omega_0) + \frac{1}{2} \phi''|_{\omega_0}(\omega - \omega_0)^2 \\ & + \frac{1}{6} \phi'''|_{\omega_0}(\omega - \omega_0)^3 + \dots \end{aligned} \quad (4)$$

The first term in this expansion is a phase constant, the second term is the group delay, and the third and fourth terms are the GDD and TOD, respectively. Our record of the interferogram does not contain information about the absolute path difference between the two arms of the interferometer; therefore our measurement provides only the GDD, TOD, and higher-order terms. However, the GDD and TOD are the most relevant terms required to analyze the dispersive effects of the Cr:forsterite in a femtosecond laser because they are the lowest-order terms responsible for pulse shaping.

It should be noted that the theory described so far does not involve a possible nonlinear refractive index of Cr:forsterite. This is certainly valid for the low power in the white-light interferometry. But for mode-locked laser operation, especially when the beam is focused into the crystal, the peak intensities can become so large that the nonlinear refractive index might also contribute to dispersion.

4. Experimental Results

Cr:forsterite is a biaxial crystal. The three different crystal axes can be specified according to the lattice

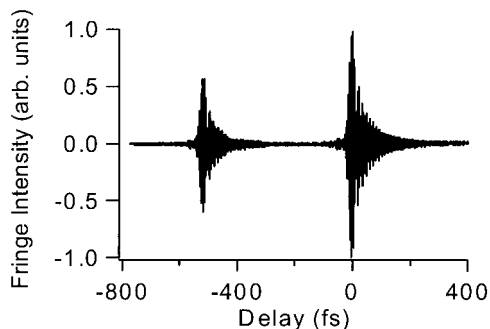


Fig. 1. Measured white-light interferogram of Cr:forsterite with unpolarized light. The two packets of fringes arise from the light polarized along the b axis (small amplitude) and c axis (large amplitude). A properly oriented polarizer before the detector is used to select one of these individual interferograms for analysis of the dispersion along the respective axis.

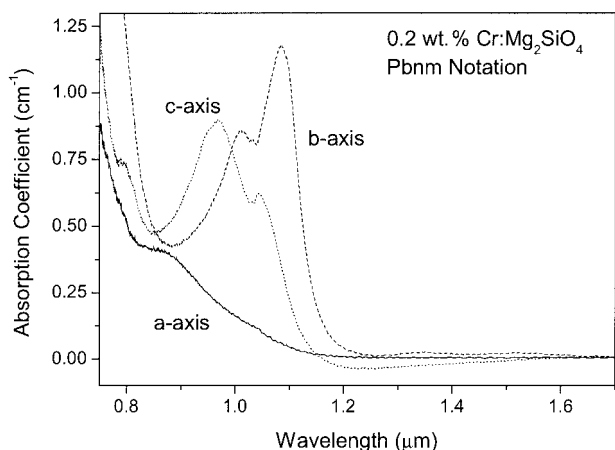


Fig. 2. Measured absorption coefficients of Cr:forsterite for light polarized along the three different crystal axes.

constants as the a axis (4.76 Å), b axis (10.22 Å), and c axis (5.99 Å). Here we use the Pbnm crystallographic notation. Our Cr:forsterite sample is $L = 5.17 \pm 0.08$ mm in length along the a axis, which is the direction the light propagated for these measurements. With unpolarized light, we can identify two white-light interferograms arising from the polariza-

tions along the b and c axes that are shown in Fig. 1. The interferogram at early delays corresponds to the light that is polarized along the b axis, whereas the second interferogram arises from the polarization along the c axis. From this measurement we can see that the difference in group delay for pulses propagating along the two axes is ~ 50 fs/mm at the peak wavelength of 1.6 μm . The crystal axes were identified by independent measurements of the polarized transmission spectrum of the Cr:forsterite sample (see Fig. 2). Between 0.9 and 1.1 μm there are distinguishing absorption bands for polarization along the b and c axes. Even a simple measurement of the transmission of a narrowband 1075-nm source along the b and c axes of our sample is sufficient to identify the two axes.

In the white-light interferometer, a broadband polarizer was used to select light that is polarized along either the b or c axis of the Cr:forsterite. For each polarization, as well as for the balanced Michelson interferometer, ten data sets were measured. After calibration of the delay axis of the Michelson interferometer, the data were Fourier transformed, and the reference phase $\phi_1(\omega)$ was subtracted to yield the phase $\phi_{\text{Cr}}(\omega - \omega_0)$, where ω_0 corresponds to 1300 nm. The data were then fitted with a fifth-order polynomial in the range from $\omega - \omega_0 = -0.3 \text{ fs}^{-1}$ to $+0.4 \text{ fs}^{-1}$ and the derivatives were taken. As is often done, we normalize ϕ_{Cr} by twice the length of the Cr:forsterite sample (i.e., $2L$). This yields the following formulas for the GDD and TOD in units of square femtoseconds per millimeter and cubic femtoseconds per millimeter, respectively:

$$\frac{\phi_{\text{Cr}}''(\omega)}{2L} = \frac{1}{2L} [2K_2 + 6K_3(\omega - \omega_0) + 12K_4(\omega - \omega_0)^2 + 20K_5(\omega - \omega_0)^3], \quad (5)$$

$$\frac{\phi_{\text{Cr}}'''(\omega)}{2L} = \frac{1}{2L} [6K_3 + 24K_4(\omega - \omega_0) + 60K_5(\omega - \omega_0)^2], \quad (6)$$

where $K_2 = 81.71 \text{ fs}^2$, $K_3 = 142.57 \text{ fs}^3$, $K_4 = -78.54 \text{ fs}^4$, and $K_5 = 23.63 \text{ fs}^5$ for the c axis; and $K_2 = 84.42$

Table 1. Measured GDD and TOD for Light Polarized Along the c and b Axes and for Wavelengths between 1050 and 1600 nm

λ (nm)	ω (fs^{-1})	GDD c Axis (fs^2/mm)	GDD b Axis (fs^2/mm)	TOD c Axis (fs^3/mm)	TOD b Axis (fs^3/mm)
1050	1.7940	35.36 ± 0.59	35.63 ± 0.72	36.14 ± 4.08	73.02 ± 4.80
1100	1.7124	32.10 ± 0.48	30.43 ± 0.51	44.20 ± 2.06	56.18 ± 2.59
1150	1.6380	28.48 ± 0.43	26.55 ± 0.42	53.15 ± 1.04	49.22 ± 1.27
1200	1.5697	24.54 ± 0.38	23.21 ± 0.37	62.69 ± 1.05	49.91 ± 0.89
1250	1.5069	20.29 ± 0.31	19.90 ± 0.32	72.60 ± 1.29	56.52 ± 1.04
1300	1.4490	15.80 ± 0.25	16.32 ± 0.27	82.70 ± 1.40	67.69 ± 1.18
1350	1.3953	11.09 ± 0.19	12.31 ± 0.23	92.87 ± 1.42	82.38 ± 1.27
1400	1.3455	6.21 ± 0.14	7.79 ± 0.18	103.03 ± 1.51	99.76 ± 1.48
1450	1.2991	1.20 ± 0.11	2.72 ± 0.13	113.09 ± 1.85	119.19 ± 1.92
1500	1.2558	-3.91 ± 0.13	-2.88 ± 0.11	123.02 ± 2.44	140.13 ± 2.59
1550	1.2153	-9.09 ± 0.22	-9.00 ± 0.18	132.77 ± 3.23	162.19 ± 3.44
1600	1.1773	-14.31 ± 0.34	-15.58 ± 0.30	142.32 ± 4.15	185.04 ± 4.41

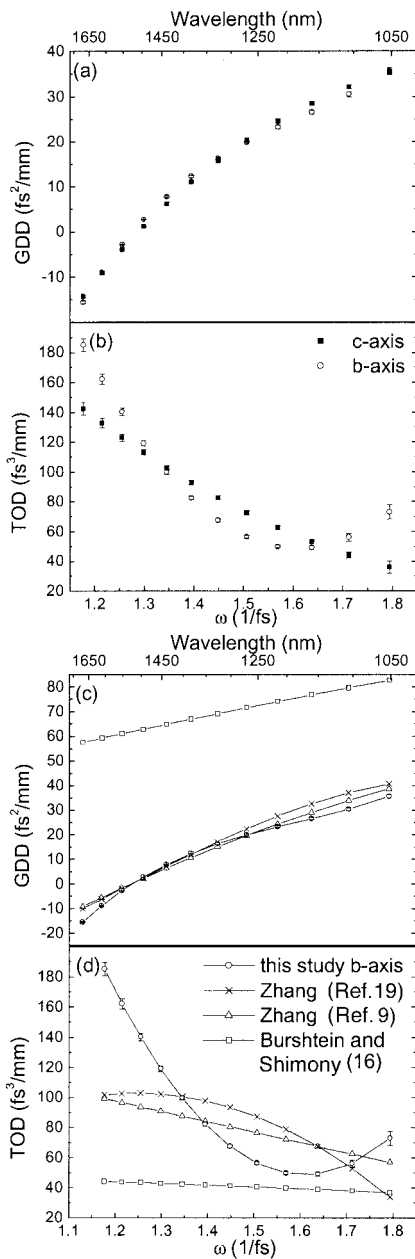


Fig. 3. Measured dispersion coefficients as a function of wavelength and frequency for polarizations along both *c* and *b* axes: (a) second-order dispersion (GDD), (b) third-order dispersion (TOD). (c) and (d) show a comparison of our GDD and TOD data with the data of Zhang *et al.*^{9,19} and Burshtein and Shimony.

fs², $K_3 = 116.70$ fs³, $K_4 = -101.21$ fs⁴, and $K_5 = 125.08$ fs⁵ for the *b* axis.

The dispersion coefficients for wavelengths from 1050 to 1600 nm were then calculated in steps of 50 nm for all data sets and the average was taken. The results are listed in Table 1 and are presented graphically in Figs. 3(a) and 3(b). Figure 3(a) shows the GDD for the *c* and *b* axes, whereas Fig. 3(b) shows the TOD along these axes. The error bars represent statistical measurement errors that are due to the variations from one measurement to the next in addition to the uncertainty in the determination of the crystal

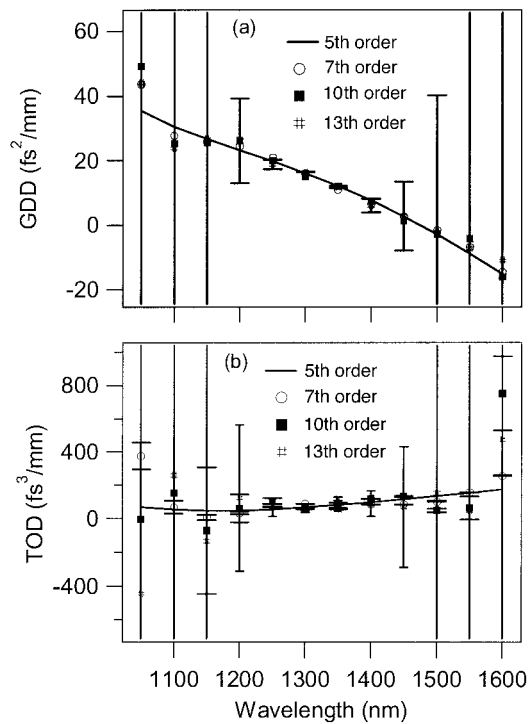


Fig. 4. Comparison of (a) GDD and (b) TOD calculated from higher-order polynomial fits for the *b* axis. Error bars are shown for all measurements and extend beyond the graphed region at short and long wavelengths.

length. The zero-GDD wavelengths that we infer from our data are $\lambda_b = 1475$ nm for the *b* axis and $\lambda_c = 1462$ nm for the *c* axis.

We did not attempt to evaluate all the systematic effects that could be present in such measurements. However, numerous repeated measurements with various alignments of the interferometer and the Cr:forsterite crystal never resulted in values that differed from the given mean values by more than twice the stated statistical uncertainty. One potential source of uncertainty is related to the polynomial fit of the phase. As stated above, we chose to use a fifth-order polynomial; however, one might envision using polynomials of even higher order. Figure 4 is a plot of the GDD and TOD for the *b* axis that are both calculated from polynomial fits to the measured phase for polynomial orders of 7, 10, and 13. For reference, the GDD and TOD obtained with the fifth-order polynomial are also shown. One finds that, over the central portion of the spectral region, the agreement between all the different order fits is quite good (<5%, 1200–1350 nm for the GDD and <30%, 1250–1400 nm for the TOD). Even further into the spectral wings the general trend of the fifth-order fit is preserved. However, the fluctuations with the higher-order polynomials (as indicated by the error bars) from one measurement to the next are much greater. We attribute this to the high-order fitting of noiselike fluctuations across the spectrum. These fluctuations are fitted by the polynomial through the balancing of large contributions (approximately 10⁷)

Table 2. Comparison of Our Measured Dispersion Data with Previously Available Data

Reference	λ (nm)	GDD (fs ² /mm)	TOD (fs ³ /mm)	Measurement Method
Sennaroglu <i>et al.</i> ^a	1230	154.16 ± 15.42	583.33 ± 58.33	<i>In situ</i> cavity dispersion measurement
Yanovsky <i>et al.</i> ^b	1275	24 ± 4	≤53	Pulse broadening
Yanovsky <i>et al.</i> ^c	1250	21.05	57.89	<i>In situ</i> cavity dispersion measurement
Zhang <i>et al.</i> ^d	1230	21.50	74.50	White-light interferometry
Zhang <i>et al.</i> ^d	1250	19.50	76.50	White-light interferometry
Zhang <i>et al.</i> ^e	1230	24.50	84.00	White-light interferometry
Zhang <i>et al.</i> ^e	1250	22.50	87.00	White-light interferometry
Burshtein and Shimony ^f	1250	71.57	40.62	Minimum-deviation measurement
This study, <i>b</i> axis	1230	21.25 ± 0.34	53.28 ± 0.98	White-light interferometry
This study, <i>b</i> axis	1250	19.9 ± 0.32	56.52 ± 1.04	White-light interferometry
This study, <i>c</i> axis	1230	22.03 ± 0.34	68.63 ± 1.19	White-light interferometry
This study, <i>c</i> axis	1250	20.29 ± 0.31	72.60 ± 1.29	White-light interferometry

^aRef. 18.

^bRef. 6.

^cRef. 17.

^dRef. 9.

^eRef. 19.

^fRef. 16.

from high-order terms to obtain a small number. In any measurement, this is generally not good practice. Furthermore, from a physical standpoint we assume the dispersion to be a smoothly varying function of frequency that is well approximated by a Taylor expansion consisting of a reasonable number of terms. Indeed the contributions of higher-order terms should be smaller and smaller corrections. If an excessive number of terms would be required to reproduce oscillations in the phase data, then our underlying assumption may need to be reevaluated.

5. Conclusion

We believe that the measurements presented here help to clarify previously published data^{4,6,9,16–19} and provide a basis for improved knowledge of the dispersion of Cr:forsterite. A summary of published data is given in Table 2, and the data of Zhang *et al.*^{9,19} and Burshtein and Shimony¹⁶ are plotted in Figs. 3(c) and 3(d) for comparison with our results. Part of the difficulty in making comparisons with previous measurements lies in the interpretation of the orientation of the Cr:forsterite crystal that others have used. Although not specified in many cases, it is reasonable to assume that all previous measurements were made for light polarized along the *b* axis, which is the most common orientation for Cr:forsterite to be used in a laser. If we assume this is the case for the results of Yanovsky *et al.*,¹⁷ then we find good agreement with our present measurements of both the GDD and the TOD for the *b* axis at 1250 nm. Note that the data of Yanovsky *et al.*¹⁷ were not taken by white-light interferometry but by an intracavity *in situ* technique; therefore the good agreement enhances the credibility of both their data and ours.

Zhang *et al.* have published two different measurements of the dispersion of Cr:forsterite.^{9,19} Although they do not state it explicitly, it appears that they used the Pnma crystallographic notation instead

of the Pbnm notation that we use. The transformation from Pnma to Pbnm is

$$\begin{aligned}
 a_{\text{Pnma}} &\rightarrow b_{\text{Pbnm}} \\
 b_{\text{Pnma}} &\rightarrow c_{\text{Pbnm}} \\
 c_{\text{Pnma}} &\rightarrow a_{\text{Pbnm}}.
 \end{aligned}
 \tag{7}$$

With this assumption, our data for the b_{Pbnm} axis can be compared with their data for the a_{Pnma} axis. Doing so, we find relatively good agreement of our measured GDD data with theirs over most of the wavelength range. For the TOD data, however, more significant differences can be seen. For example, at 1250 nm our results are 35% and 50% smaller than those reported in the two publications of Zhang *et al.*^{9,19} It is unlikely that this disagreement is due to differences in doping concentration because the host-crystal properties dominate; however, it is not known how strongly the GDD and TOD depend on other factors related to the purity of the host crystal. We have also computed the GDD and TOD from the recent index of refraction data of Burshtein and Shimony.¹⁶ As can be seen in Figs. 3(c) and 3(d), the GDD values show little agreement with any of the other studies, whereas the TOD values are at least comparable to ours and the other published measurements.

In summary, we have presented thorough measurements of the GDD and TOD of Cr:forsterite from 1050 to 1600 nm along the *b* and *c* axes of the crystal. To clarify previous results, careful attention has been paid to the orientation of the Cr:forsterite crystal. Our measurements give a basis for optimization of dispersion control in femtosecond Cr:forsterite lasers and should also prove useful in the construction of analytic expressions for the index of refraction of Cr:forsterite that are just now beginning to be formulated.¹⁶ In addition to our data, this requires the measurement of both the absolute refractive index

and the first derivative $dn/d\lambda$ at one specific wavelength.

References

1. V. Petricevic, S. K. Gayen, R. R. Alfano, K. Yamagishi, H. Anzai, and Y. Yamaguchi, "Laser action in chromium-doped forsterite," *Appl. Phys. Lett.* **52**, 1040–1042 (1988).
2. A. Seas, V. Petricevic, and R. R. Alfano, "Generation of sub-100-fs pulses from a cw mode-locked chromium-doped forsterite laser," *Opt. Lett.* **17**, 937–939 (1992).
3. A. Sennaroglu, T. J. Carrig, and C. R. Pollock, "Femtosecond pulse generation by using an additive-pulse mode-locked chromium-doped forsterite laser operated at 77 K," *Opt. Lett.* **17**, 1216–1218 (1992).
4. A. Sennaroglu, C. R. Pollock, and H. Nathel, "Generation of 48-fs pulses and measurement of crystal dispersion by using a regeneratively initiated self-mode-locked chromium-doped forsterite laser," *Opt. Lett.* **18**, 826–828 (1993).
5. A. Seas, V. Petricevic, and R. R. Alfano, "Self-mode-locked chromium-doped forsterite laser generates 50-fs pulses," *Opt. Lett.* **18**, 891–893 (1993).
6. V. Yanovsky, Y. Pang, F. Wise, and B. Minkov, "Generation of 25-fs pulses from a self-mode-locked Cr:forsterite laser with optimized group-delay dispersion," *Opt. Lett.* **18**, 1541–1543 (1993).
7. Y. P. Tong, P. M. W. French, J. R. Taylor, and J. G. Fujimoto, "All-solid-state femtosecond sources in the near-infrared," *Opt. Commun.* **136**, 235–238 (1997).
8. X. Liu, L. Quian, F. Wise, Z. Zhang, T. Itatani, T. Sugaya, T. Nakagawa, and K. Torizuka, "Femtosecond Cr:forsterite laser diode pumped by a double-clad fiber," *Opt. Lett.* **23**, 129–131 (1998).
9. Z. Zhang, K. Torizuka, T. Itatani, K. Kobayashi, T. Sugaya, and T. Nakagawa, "Self-starting mode-locked femtosecond forsterite laser with a semiconductor saturable-absorber mirror," *Opt. Lett.* **22**, 1006–1008 (1997).
10. B. E. Bouma, G. J. Tearney, I. P. Bilinsky, B. Golubovic, and J. G. Fujimoto, "Self-phase-modulated Kerr-lens mode-locked Cr:forsterite laser source for optical coherence tomography," *Opt. Lett.* **21**, 1839–1841 (1996).
11. V. V. Yakovlev, V. Shcheslavskiy, and A. Ivanov, "High-energy femtosecond Cr:forsterite oscillators and their applications in biomedical and material sciences," *Appl. Phys. B* **74**, S145–S152 (2002).
12. S. A. Diddams, D. J. Jones, J. Ye, S. T. Cundiff, J. L. Hall, J. K. Ranka, R. S. Windeler, R. Holzwarth, Th. Udem, and T. W. Hänsch, "A direct link between microwave and optical frequencies with a 300 THz femtosecond laser comb," *Phys. Rev. Lett.* **84**, 5102–5105 (2000).
13. R. Shelton, L. Ma, H. Kapteyn, M. Murnane, J. Hall, and J. Ye, "Phase-coherent optical pulse synthesis from separate femtosecond lasers," *Science* **293**, 1286–1289 (2001).
14. Z. Wei, Y. Kobayashi, Z. Zhang, and K. Torizuka, "Generation of two-color femtosecond pulses by self-synchronizing Ti:sapphire and Cr:forsterite lasers," *Opt. Lett.* **26**, 1806–1808 (2001).
15. C. Chudoba, J. G. Fujimoto, E. P. Ippen, H. A. Haus, U. Morgner, F. X. Kaertner, V. Scheuer, G. Angelow, and T. Tschudi, "All-solid-state Cr:forsterite laser generating 14-fs pulses at 1.3 μm ," *Opt. Lett.* **26**, 292–294 (2001).
16. Z. Burshtein and Y. Shimony, "Refractive index dispersion and anisotropy in $\text{Cr}^{4+}:\text{Mg}_2\text{SiO}_4$," *Opt. Mater.* **20**, 87–96 (2002).
17. V. Yanovsky, Y. Pang, and F. Wise, "Self-modelocked Cr:forsterite laser with optimized group-delay dispersion," in *Generation, Amplification and Measurement of Ultrashort Laser Pulses*, R. P. Trebino and I. A. Walmsley, eds., *Proc. SPIE* **2116**, 293–299 (1993).
18. A. Sennaroglu, C. R. Pollock, and H. Nathel, "Generation of tunable femtosecond pulses in the 1.21–1.27 μm and 605–635 nm wavelength regime by using a regeneratively initiated self-mode-locked Cr:forsterite laser," *IEEE J. Quantum Electron.* **30**, 1851–1861 (1994).
19. Z. Zhang, K. Torizuka, T. Itatani, K. Kobayashi, T. Sugaya, and T. Nakagawa, "Femtosecond Cr:forsterite laser with mode locking initiated by a quantum-well saturable absorber," *IEEE J. Quantum Electron.* **33**, 1975–1981 (1997).
20. K. Naganuma, K. Mogi, and H. Yamada, "Group-delay measurement using the Fourier transform of an interferometric cross correlation generated by white light," *Opt. Lett.* **15**, 393–395 (1993).
21. S. Diddams and J.-C. Diels, "Dispersion measurements with white-light interferometry," *J. Opt. Soc. Am. B* **13**, 1120–1129 (1996).
22. A. G. Van Engen, S. A. Diddams, and T. S. Clement, "Dispersion measurements of water with white-light interferometry," *Appl. Opt.* **37**, 5679–5686 (1998).